

Enhanced anomalous Hall effect in kagome magnet $YbMn_6Sn_6$ with intermediate-valence ytterbium

Longfei Li(李龙飞), Shengwei Chi(迟晟玮), Wenlong Ma(马文龙), Kaizhen Guo(郭凯臻), Gang Xu(徐刚), and Shuang Jia(贾爽)

Citation: Chin. Phys. B, 2024, 33 (**5**): 057501. DOI: 10.1088/1674-1056/ad322d
Journal homepage: http://cpb.iphy.ac.cn; http://iopscience.iop.org/cpb

What follows is a list of articles you may be interested in

Angular and planar transport properties of antiferromagnetic V_5S_8

Xiao-Kai Wu(吴晓凯), Bin Wang(王彬), De-Tong Wu(吴德桐), Bo-Wen Chen(陈博文), Meng-Juan Mi(弭孟娟), Yi-Lin Wang(王以林), and Bing Shen(沈冰)
Chin. Phys. B, 2024, 33 (**2**): 027503. DOI: 10.1088/1674-1056/ad15f9

Anomalous Hall effect in ferromagnetic $LaCo_2As_2$ and ferrimagnetic $NdCo_2As_2$

Yu-Qing Huang(黄雨晴), Peng-Yu Zheng(郑鹏宇), Rui Liu(刘瑞), Xi-Tong Xu(许锡童), Zi-Yang Wu(吴紫阳), Chao Dong(董超), Jun-Feng Wang(王俊峰), Zhi-Ping Yin(殷志平), and Shuang Jia(贾爽)
Chin. Phys. B, 2023, 32 (**10**): 107502. DOI: 10.1088/1674-1056/acd925

Magnetic and electronic properties of bulk and two-dimensional $FeBi_2Te_4$: A first-principles study

Qianqian Wang(王倩倩), Jianzhou Zhao(赵建洲), Weikang Wu(吴维康), Yinning Zhou(周胤宁), Qile Li, Mark T. Edmonds, and Shengyuan A. Yang(杨声远)
Chin. Phys. B, 2023, 32 (**8**): 087506. DOI: 10.1088/1674-1056/acd522

Topological magnetotransport and electrical switching of sputtered antiferromagnetic $Ir_{20}Mn_{80}$

Danrong Xiong(熊丹荣), Yuhao Jiang(蒋宇昊), Daoqian Zhu(朱道乾), Ao Du(杜奥), Zongxia Guo(郭宗夏), Shiyang Lu(卢世阳), Chunxu Wang(王春旭), Qingtao Xia(夏清涛), Dapeng Zhu(朱大鹏), and Weisheng Zhao(赵巍胜)
Chin. Phys. B, 2023, 32 (**5**): 057501. DOI: 10.1088/1674-1056/acb9ec

Enhancement of spin-orbit torque efficiency by tailoring interfacial spin-orbit coupling in Pt-based magnetic multilayers

Wenqiang Wang(王文强), Gengkuan Zhu(朱耿宽), Kaiyuan Zhou(周恺元), Xiang Zhan(战翔), Zui Tao(陶醉), Qingwei Fu(付清为), Like Liang(梁力克), Zishuang Li(李子爽), Lina Chen(陈丽娜), Chunjie Yan(晏春杰), Haotian Li(李浩天), Tiejun Zhou(周铁军), and Ronghua Liu(刘荣华)
Chin. Phys. B, 2022, 31 (**9**): 097504. DOI: 10.1088/1674-1056/ac76aa

---

SPECIAL TOPIC — Recent progress on kagome metals and superconductors

Enhanced anomalous Hall effect in kagome magnet $YbMn_6Sn_6$ with intermediate-valence ytterbium

Longfei Li(李龙飞)[1], Shengwei Chi(迟晟玮)[2], Wenlong Ma(马文龙)[1], Kaizhen Guo(郭凯臻)[1], Gang Xu(徐刚)[2], and Shuang Jia(贾爽)[1,3,4,†]

[1] *International Center for Quantum Materials, School of Physics, Peking University, Beijing* 100871, *China*
[2] *Wuhan National High Magnetic Field Center and School of Physics, Huazhong University of Science and Technology, Wuhan* 430074, *China*
[3] *Interdisciplinary Institute of Light-Element Quantum Materials and Research Center for Light-Element Advanced Materials, Peking University, Beijing* 100871, *China*
[4] *Hefei National Laboratory, Hefei* 230088, *China*

(Received 19 January 2024; revised manuscript received 28 February 2024; accepted manuscript online 11 March 2024)

We report on the magnetization and anomalous Hall effect (AHE) in the high-quality single crystals of the kagome magnet $YbMn_6Sn_6$, where the spins of the Mn atoms in the kagome lattice order ferromagnetically and the intermediate-valence Yb atoms are nonmagnetic. The intrinsic mechanism plays a crucial role in the AHE, leading to an enhanced anomalous Hall conductivity (AHC) compared with the other rare-earth RMn_6Sn_6 compounds. Our band structure calculation reveals a strong hybridization between the 4f electrons of Yb and conduction electrons.

Keywords: anomalous Hall effect, kagome magnet, intermediate valence

PACS: 75.47.–m, 72.15.Eb, 71.20.Lp **DOI:** 10.1088/1674-1056/ad322d

1. Introduction

Kagome magnets have been a subject of significant interest in condensed matter physics due to their unique combination of a nontrivial geometric lattice and strong electron correlation.[1,2] The kagome lattice comprises corner-sharing triangles, which naturally lead to geometric frustration and a topological band structure, characterized by the Dirac cone and flat band. These distinctive structures in both real and reciprocal spaces make the kagome materials an intriguing platform for exploring topological states and phenomena, including quantum spin liquid[3] and the long-pursued high-temperature quantum anomalous Hall effect.[4,5]

The RMn_6Sn_6 compounds, which include rare-earth elements represented by R, belong to a grand family of intermetallic compounds with the chemical formula RT_6E_6 (T = transition metals including V, Cr, Mn, Fe, Co, Ni, and E = Ga, Ge, In, Sn, Sb). The crystal structure of RMn_6Sn_6 consists of transition-metal-based kagome lattice, either pristine or distorted depending on the arrangement of R.[6–8] $LiMn_6Sn_6$, $MgMn_6Sn_6$, and RMn_6Sn_6 (R = Gd–Tm, Lu) compounds crystallize in the $HfFe_6Ge_6$-type structure (space group $P6/mmm$), which can be regarded as an alternatively R-stuffed CoSn-type structure.[6,7] This simple ordered alteration of R-occupied with R-vacant honeycombs leads to the formation of the pristine Mn-based kagome lattice (see inset in Fig. 1). The magnetic properties of RMn_6Sn_6 are determined by the magnetic interactions and anisotropy of both Mn and R atoms.[8] The intralayer Mn–Mn interaction is the strongest, leading the Mn kagome lattice to form an in-plane ferromagnetic (FM) order. When the R atom is nonmagnetic, the valence electron count (VEC) plays a crucial role on the interlayer magnetic interactions, leading to an easy-plane FM structure for monovalent $LiMn_6Sn_6$ and divalent $MgMn_6Sn_6$,[9–11] a complex antiferromagnetic (AFM) spiral structure for trivalent Sc(Y,Lu)Mn_6Sn_6,[12] and a helical structure for tetravalent Zr(Hf)Mn_6Sn_6.[13] For magnetic R elements, the R–Mn interaction controls the magnetic order and anisotropy. Light rare-earth Nd and Sm sublattice orders simultaneously with the Mn sublattice, resulting in an FM order.[14] For heavy rare-earth elements Gd, Tb, Dy, and Ho, the R moment orders antiparallel with respect to the Mn moment, leading to a ferrimagnetic (FiM) order. The R–Mn interaction is too weak for R elements being Er and Tm, causing these two members to revert to an AFM order.[15,16]

Recent studies have reported significant anomalous Hall effect (AHE) and topological Hall effect (THE) in the RMn_6Sn_6 compounds. Of particular, the FiM compound $TbMn_6Sn_6$ shows a pronounced intrinsic AHE stemming from a strong Berry curvature field of a massive Dirac fermion with a significant Chern gap in the Mn-based kagome lattice.[17,18] This highly nontrivial topological electron structure also produces intrinsic AHE in the FiM state of Gd, Dy, Ho, and Er sibling compounds.[19] The light rare-earth Nd(Sm)Mn_6Sn_6 with an FM structure also demonstrates an intrinsic AHE with similar magnitude.[20] On the other hand, the flat spiral magnetic

†Corresponding author. E-mail: gwljiashuang@pku.edu.cn

© 2024 Chinese Physical Society and IOP Publishing Ltd

structure of YMn_6Sn_6 can gradually change to a non-collinear, fan structure when an external magnetic field is applied in the plane, leading to a significant THE.[21,22] The studies on the AHE and THE indicate that the RMn_6Sn_6 family has the potential to be a model system for examining the relationship between the geometric frustration and non-trivial topological band structure of the kagome lattice.

It has been noticed that $YbMn_6Sn_6$ possesses different crystal and magnetic properties from the other heavy rare-earth RMn_6Sn_6 compounds. It crystallizes in an intermediate ordered state between the $HfFe_6Ge_6$- and YCo_6Ge_6-type structures, as previously found in $SmMn_6Sn_6$.[10,14,23] Thermodynamic and neutron scattering measurements revealed that the Mn sublattices order ferromagnetically in the plane at a relatively low Curie temperature $T_C \sim 277$ K while the Yb atoms have no magnetic moment.[24,25] X-ray absorption near edge structure (XANES) and resonant inelastic x-ray scattering (RIXS) measurements revealed that the Yb atom has a non-integer valence between 2+ and 3+.[24,26] This intermediate valence of Yb atoms well explains the fact that its magnetic properties are similar to those of divalent $MgMn_6Sn_6$ rather than the other trivalent rare-earth RMn_6Sn_6 compounds.

The discovery of the topological electronic structure and AHE in RMn_6Sn_6 compounds motivates us to examine the electronic and magnetic properties of single-crystalline $YbMn_6Sn_6$. Although the polycrystalline samples of $YbMn_6Sn_6$ have been extensively studied, the physical properties of single crystals remain largely unexplored. During the preparation of the manuscript, we noticed the study in Ref. [27], which reported the electric transport properties of the $YbMn_6Sn_6$ single crystals when a magnetic field was applied along the c axis. In the current study, we report a successful growth of large, high-quality single crystals of $YbMn_6Sn_6$ and their magnetic and electric transport properties. We observe an enhanced AHE with the anomalous Hall conductivities (AHCs) as large as 182 $\Omega^{-1}\cdot cm^{-1}$ and 922 $\Omega^{-1}\cdot cm^{-1}$ at 2 K when the saturated magnetization (M_{sat}) is along the crystallographic c axis and ab plane, respectively. Scaling analysis reveals that the intrinsic mechanism is dominant when M_{sat} is along the c axis. The intrinsic AHC is comparable to that for $TbMn_6Sn_6$ but much larger than that for non-4f-magnetic YMn_6Sn_6 and $LuMn_6Sn_6$. Our DFT calculation is partially consistent with the experimental results of intrinsic AHE. It indicates that the 4f electronic bands of Yb in the vicinity of the Fermi level play an important role in the electronic structure of $YbMn_6Sn_6$.

2. Methods

We grew the single crystals of $YbMn_6Sn_6$ by the self-flux method.[28] The Yb ingots, Mn ingots, and Sn ingots were mixed in a molar ratio of 1 : 6 : 20 and placed in an alumina crucible. The crucible was then sealed in a quartz ampoule. The ampoule was slowly heated to 1223 K, kept for 10 hours, cooled to 1073 K and held for 67 hours. It was then cooled down to 873 K and the flux was centrifuged. The obtained single crystals were etched with dilute HCl solution to remove the remnant Sn flux on the surface. Typical $YbMn_6Sn_6$ single crystals are millimeter-sized hexagonal prisms with a metallic luster (inset of Fig. 1(c)). The crystal structure of $YbMn_6Sn_6$ was examined by powder x-ray diffraction (PXRD) using a Bruker D8 Advance diffractometer with Cu K_α radiation.

We confirmed the intermediate crystal structure of $YbMn_6Sn_6$ between the $HfFe_6Ge_6$- and YCo_6Ge_6-type structures, as reported in Refs. [10,23]. The difference between these two structures lies in the distribution of the Yb atoms: the Yb atoms alternatively occupy the slab along the c axis in the $HfFe_6Ge_6$-type structure while randomly distribute in the two slabs in the YCo_6Ge_6-type structure. As a result, the unit cell of the $HfFe_6Ge_6$-type structure doubles that of the YCo_6Ge_6-type structure along the c axis, which leads to distinctive PXRD pattern. The diffraction peaks with the Miller indices (hkl) in the $HfFe_6Ge_6$-type structure are absent in the YCo_6Ge_6-type structure when l is an odd integer. As shown in Fig. 1(c), the intensities of the diffraction peaks with indices $(hk3)$ are about 40% of those for a fully ordered $HfFe_6Ge_6$-type structure, indicating an intermediate ordered state, as that for $SmMn_6Sn_6$ annealed at 723 K in Ref. [14].

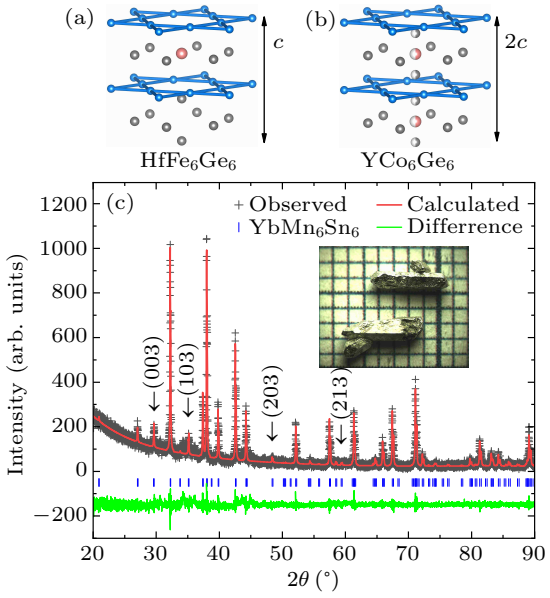


Fig. 1. (a) $HfFe_6Ge_6$-type and (b) YCo_6Ge_6-type crystal structures, where the Mn-based kagome lattices are highlighted as blue. Pink spheres: Yb atoms; gray spheres: Sn atoms. Note that in the YCo_6Ge_6-type structure the Yb and Sn atoms are mixed. (c) Refined PXRD data of $YbMn_6Sn_6$ single crystals, where the black crosses are the measured values and the red curve is the calculated pattern. The vertical blue bars are the expected peak positions. Note that the Miller indices $(hk3)$ are labeled. Inset: $YbMn_6Sn_6$ single crystals with typical sample morphology of hexagonal prisms. The lateral edges are along the crystallographic c axis.

Using the Rietveld method, we refined the lattice con-

stants as $a = 5.548(6)$ Å and $c = 9.044(2)$ Å, which are significantly larger than the lattice constants of $TmMn_6Sn_6$ ($a = 5.514$ Å and $c = 8.994$ Å)[29] and $LuMn_6Sn_6$ ($a = 5.505$ Å and $c = 8.988$ Å).[24] The deviation of the lattice constants from the Lanthanide contraction indicates the intermediate valence of the Yb ions.

We measured the magnetic properties of the single crystals using the Quantum Design magnetic property measurement system (MPMS-3) when the magnetic field was applied along the crystallographic c axis and ab plane. Longitudinal and Hall resistances were measured with the Quantum Design physical property measurement system (PPMS-9) using the standard four-probe method. Small signals at low temperatures were collected by the Lake Shore Model 372 AC resistance bridge.

To obtain the electronic structure and Berry curvature field of $YbMn_6Sn_6$, we performed first-principles calculations based on density functional theory (DFT) by the Vienna *ab initio* simulation package (VASP).[30,31] A plane-wave basis set was used with the projector augmented wave method[32] with an energy cutoff of 400 eV. The Brillouin zone (BZ) integration was performed using a $9 \times 9 \times 5$ Monkhorst–Pack k mesh, and generalized-gradient approximation (GGA) by Perdew, Burke, and Ernzerhof[33] was used for the exchange–correlation functional. The electronic correlation effect among Mn 3d electrons was treated with the GGA plus Hubbard U approach,[34] where $U_{\mathrm{Mn}} = 0.4$ eV. The spin–orbit coupling (SOC) was included in all the calculations. Maximally localized Wannier functions obtained from the WANNIER90 package[35] were used to derive the tight-binding model. The 4f orbitals of Yb atoms were viewed as core orbitals in the calculation of AHC. The AHC was obtained by integrating the Berry curvature according to the formula

$$\sigma_{\alpha\beta} = -\frac{e^2}{\hbar}\int_{\mathrm{BZ}}\frac{\mathrm{d}\boldsymbol{k}}{(2\pi)^3}\sum_n f(\varepsilon_{n\boldsymbol{k}})\Omega_{n,\alpha\beta}(\boldsymbol{k}),$$

where $\Omega_{n,\alpha\beta}(\boldsymbol{k}) = -\mathrm{Im}\langle\partial_\alpha u_{n\boldsymbol{k}}|\partial_\beta u_{n\boldsymbol{k}}\rangle$ is the Berry curvature of band n with momentum $\boldsymbol{k}$, f is the Fermi distribution function, and $u_{n\boldsymbol{k}}$ is the Bloch function. The integration was performed on a $251\times251\times251$ mesh using the WannierTools package.[36]

3. Results and analysis

Figure 2(a) shows the temperature dependence of the magnetization for two pieces of $YbMn_6Sn_6$ single crystals in a temperature range from 2 K to 300 K when an external magnetic field $\mu_0 H = 0.1$ T is applied along the crystallographic c axis and the ab plane, respectively. The magnetization for $H \parallel ab$ plane is over four times that of $H \parallel c$ axis, indicating an easy-plane anisotropy. According to the $M(T)$ curves, $YbMn_6Sn_6$ undergoes an FM transition at $T_{\mathrm{C}} \sim 277$ K, in agreement with previously reported results.[24,25] In the temperatures below T_{C}, the magnetization in both directions remains almost constant with decreasing temperature. The magnetization is easily saturated in low external magnetic fields for the two samples at 2 K, indicating a soft magnet with small anisotropy, in contrast to the other RMn_6Sn_6 with magnetic R. The saturated magnetization M_{sat} in both directions is about 14.5 μ_{B}/f.u.. Considering that Yb has an intermediate valence and no magnetic moment, we infer that the saturated moments for each Mn atom is about 2.4 μ_{B}, which is slightly larger than the values of the other RMn_6Sn_6 compounds.

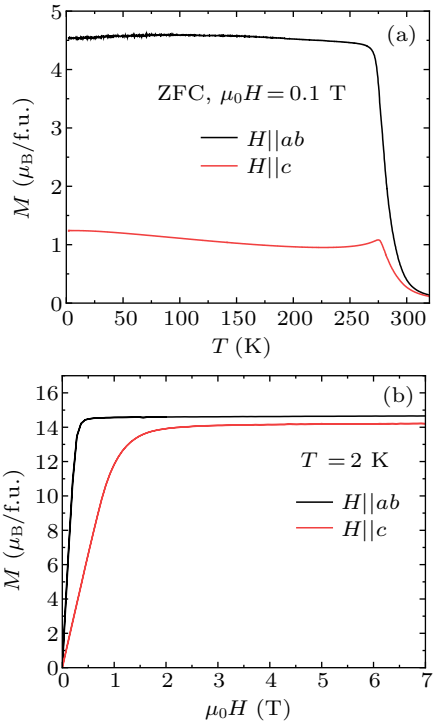


Fig. 2. Magnetization of $YbMn_6Sn_6$ single crystals. (a) $M(T)$ when an external magnetic field $\mu_0 H = 0.1$ T is along the crystallographic c axis and the ab plane, respectively. (b) $M(H)$ curves at $T = 2$ K when $H \parallel ab$ and $H \parallel c$, respectively. The slight difference in the saturated magnetization may be caused by the uncertainty of the mass for different samples.

Figure 3 shows the temperature dependence of the zero-field longitudinal resistivity $\rho(T)$ for two pieces of crystals where the electric current is applied along the c axis and the ab plane, respectively. The $\rho(T)$ has a metallic profile with a slope change at ~ 277 K, and coincidences with the T_{C}. The residual resistivity ratio $RRR = \rho(300\ \mathrm{K})/\rho(2\ \mathrm{K})$ is over 10 in both directions, indicating the high quality of our samples. The ratio of the longitudinal resistivity (ρ_{xx}/ρ_{zz}) increases from 1.3 at $T = 300$ K to 2.3 at $T = 2$ K. Considering the dimensional uncertainty of the samples, we infer that the longitudinal electric transport properties are close to isotropic.

We also measured the heat capacity for two pieces of $YbMn_6Sn_6$ and $LuMn_6Sn_6$ crystals and the data are presented in the inset of Fig. 3. Their specific heat follows the expected form of $\gamma T + \beta T^3$ for a Fermi liquid where γ is the electronic

specific heat coefficient and βT^3 is the phonon contribution. The γ value of $YbMn_6Sn_6$ (127 mJ·mol^{-1}·K^{-2}) is significantly higher than that of $LuMn_6Sn_6$ (48 mJ·mol^{-1}·K^{-2}) in which the Lu atoms have a full shell 4f electronic configuration. The γ value of $YbMn_6Sn_6$ is comparable to that of most heavy fermion materials.[37]

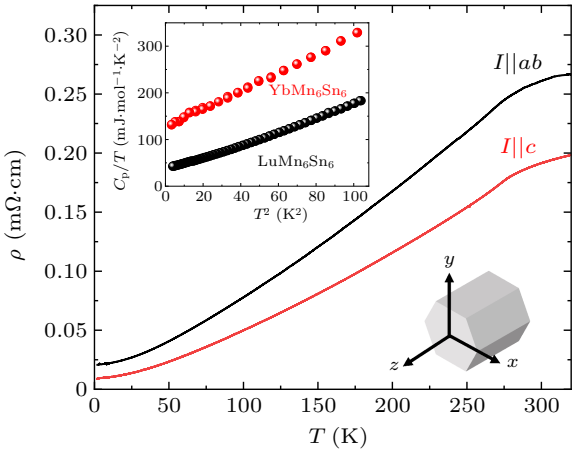


Fig. 3. Temperature dependence of the zero-field longitudinal resistivity $\rho(T)$ for two pieces of $YbMn_6Sn_6$ single crystals when the current is applied along the crystallographic c axis and the ab plane, respectively. Top inset: The specific heat of $YbMn_6Sn_6$ and $LuMn_6Sn_6$ single crystals in a form of C_p/T versus T^2. Bottom inset: Sample setup for the electric transport experiments.

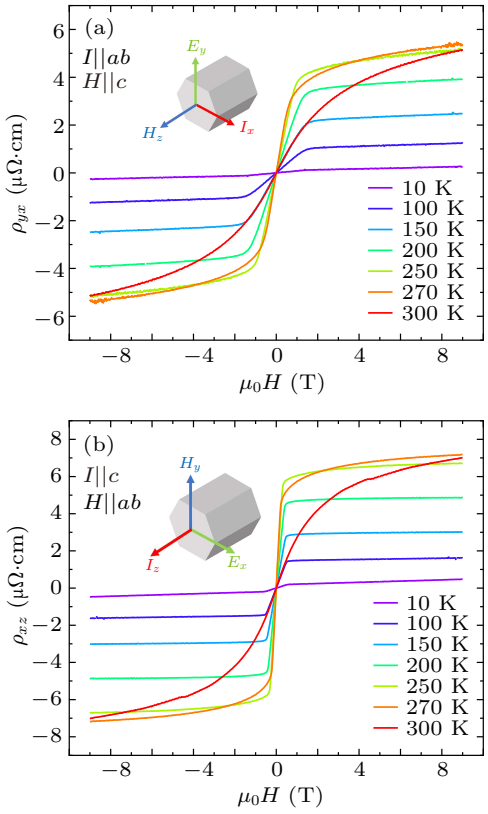


Fig. 4. Hall resistivity $\rho_{ij}(H)$ for two pieces of $YbMn_6Sn_6$ single crystals at different temperatures when an external magnetic field is applied along (a) the c axis ($\rho_{ij}=\rho_{yx}$) and (b) the ab plane ($\rho_{ij}=\rho_{xz}$). Insets: Sample setup for the electric transport experiments. Under the convention $E_i=\rho_{ij}I_j$, the external magnetic field is along the k axis of a right-handed coordinate system with i, j and k as bases, the current I is along the j axis and the electric field E from the Hall effect is along the i axis. Note that $\hat{I}\times\hat{E}=\hat{H}$.

Figures 4(a) and 4(b) show the Hall resistivity $\rho_{ij}(H)$ isotherms for two pieces of $YbMn_6Sn_6$ single crystals at representative temperatures when the external magnetic field is along the c axis and the ab plane, respectively. Note that we use the convention $E_i=\rho_{ij}I_j$, which means ρ_{yx} is positive for hole carriers when the current is along the x axis and the field is along the z axis. The coordinate system for the electric transport experiments is shown in the insets of Figs. 3 and 4. The Hall resistivity $\rho_{ij}(H)$ is composed of an ordinary part and an anomalous part, $\rho_{ij}(H)=\rho_{OH}(H)+\rho_{AH}(M)$, and the similar profiles of $\rho_{ij}(H)$ and $M(H)$ indicate that the anomalous Hall contribution is dominant.

We then collected the ρ_{AH} values as the intercept of the linear part of $\rho_{ij}(H)$ as long as the magnetization is saturated. The AHE has both intrinsic and extrinsic origins and scales with both the zero-field longitudinal resistivity ρ and the saturated magnetization $M(T)$ as[38,39]

$$\rho_{AH}=M(T)\cdot(\sigma^{int}\cdot\rho^2+\alpha^{skew}\cdot\rho). \tag{1}$$

The coefficients of the first and second power terms of the ρ are the intrinsic and extrinsic anomalous Hall coefficients, respectively. To gain insight into the scaling relation, ρ and $M(T)$ are divided into both sides. For the simplicity of the units, $M(T)$ is replaced by a dimensionless quantity, namely, a normalized magnetization $(M(T)/M_{sat})$. Note that we use the $M(T)$ values measured at $\mu_0H=2$ T, where M has been saturated in both directions. The scaling relation now reads

$$(\rho_{AH}/\rho)\cdot[M(T)/M_{sat}]^{-1}=\sigma^{int}\cdot\rho+\alpha^{skew}. \tag{2}$$

We plot $(\rho_{AH}/\rho)\cdot[M(T)/M_{sat}]^{-1}$ against ρ in Figs. 5(a) and 5(b) for the electric current in the ab plane and c axis, respectively, and perform a linear fit for the data of temperatures below T_C. Note that for the external magnetic field applied along the c axis, the temperature range of the linear fit has been restricted to below 230 K to reduce the influence of strong magnetic fluctuations around the magnetic transition temperature. The intrinsic and extrinsic anomalous Hall coefficients are the slope and the intercept, respectively. We obtain the intrinsic AHC as $\sigma_{xy}^{int}=146.3\ \Omega^{-1}\cdot cm^{-1}$ for $H\parallel c$ axis and $\sigma_{zx}^{int}=307.9\ \Omega^{-1}\cdot cm^{-1}$ for $H\parallel ab$ plane. Given the lattice constant $c=9.044(2)$ Å, the intrinsic AHC σ_{xy}^{int} corresponds to $0.155e^2/h$ per kagome layer, which is comparable to the intrinsic AHC for $TbMn_6Sn_6$.[19]

To understand the role the 4f electrons in $YbMn_6Sn_6$ played by in the AHE, we comparably studied the non-4f counterpart YMn_6Sn_6 single crystal. YMn_6Sn_6 crystallizes in the $HfFe_6Ge_6$-type structure and has a double-flat-spiral magnetic structure as the ground state in which the Mn spins in each kagome bilayer are collinear ferromagnetically within the plane and form helical stacking of the FM bilayers.[12] The magnetic structure can be driven to a forced ferromagnetic (FF) state by an external field along the c axis.[22] As shown in Fig. 6, the Hall resistivity of YMn_6Sn_6 follows the $M(H)$

curves at representative temperatures from 100 K to 300 K. We extracted the anomalous Hall resistivity $\rho_{\rm AH}$ of the FF state as the intercept of the linear part of $\rho_{yx}(H)$. The scaling law $\rho_{\rm AH} = \sigma^{\rm int} \cdot \rho^2 + \alpha^{\rm skew} \cdot \rho$ yields an intrinsic AHC $\sigma_{xy}^{\rm int} = 24\ \Omega^{-1}{\cdot}{\rm cm}^{-1}$ for YMn_6Sn_6, which is much smaller than that in $YbMn_6Sn_6$.

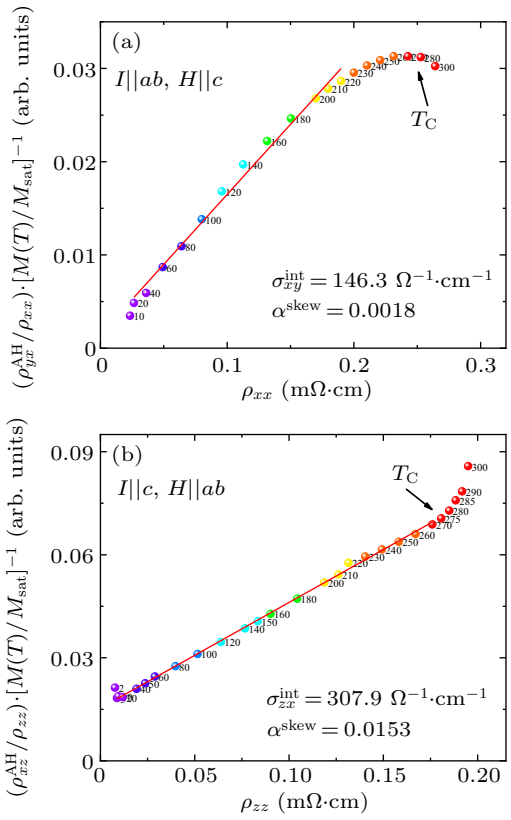


Fig. 5. Scaling of the AHE for two pieces of $YbMn_6Sn_6$ crystals when an external magnetic field is applied along (a) the *c* axis and (b) the *ab* plane. Temperatures are labeled to the right of each data point.

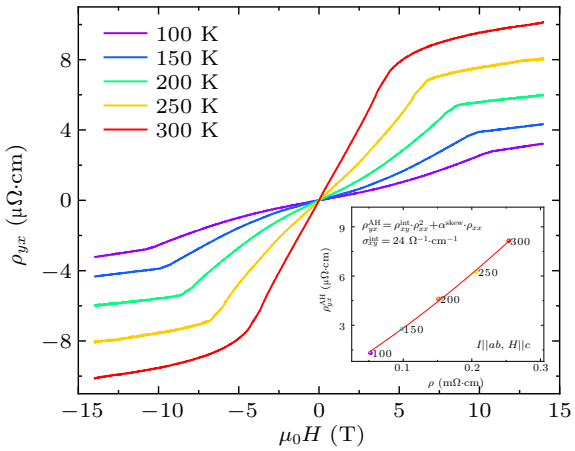


Fig. 6. Hall resistivity $\rho_{yx}(H)$ of YMn_6Sn_6 single crystal at selective temperatures when an external magnetic field is applied along the *c* axis. Inset: Scaling law reveals that the intrinsic AHC in YMn_6Sn_6 is 24 $\Omega^{-1}{\cdot}{\rm cm}^{-1}$.

To verify the validity of the scaling between $\rho_{\rm AH}$ and ρ in $YbMn_6Sn_6$, we also scale the AHC and the squares of longitudinal conductivity in Fig. 7 for four pieces of samples. When $M_{\rm sat}$ is along the *c* axis, the AHC $\sigma_{xy}^{\rm AH}$ remains constant for higher longitudinal conductivity σ_{xx} at low temperatures. This value is close to the intrinsic anomalous Hall coefficient $\sigma_{xy}^{\rm int}$ we obtained from the scaling between $\rho_{\rm AH}$ and ρ, indicating the main contribution from the intrinsic mechanism. On the other hand, the AHC $\sigma_{zx}^{\rm AH}$ increases with higher longitudinal conductivity σ_{zz} at low temperatures when $M_{\rm sat}$ is in the *ab* plane, indicating that the extrinsic mechanism plays an important role. These results are consistent with each other for different pieces of samples.

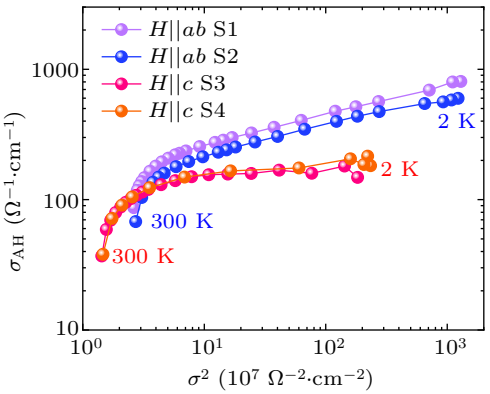


Fig. 7. Scaling of the AHC in different crystallographic directions against the square of the longitudinal conductivity in a temperature range from 2 K to 300 K.

4. Discussion

In order to better understand the intermediate-valence Yb and the AHE in $YbMn_6Sn_6$, we performed DFT calculations to obtain the band structure and the intrinsic AHC. We chose the fully ordered $HfFe_6Ge_6$-type structure and the lattice constants obtained from the experiments. As shown in Fig. 8, the energetic dispersion is highlighted by a flat band only 0.2 eV below the Fermi energy. The bands consisting of Yb orbitals have a strong hybridization with the conduction electrons. The band structures near the Fermi energy originating from the Mn kagome layers exhibit striking similarities with those of other RMn_6Sn_6 compounds. In particular, the Dirac cones located at the *K*-points in the Brillouin zones are especially reminiscent of those found in other RMn_6Sn_6 compounds.[17,40–42]

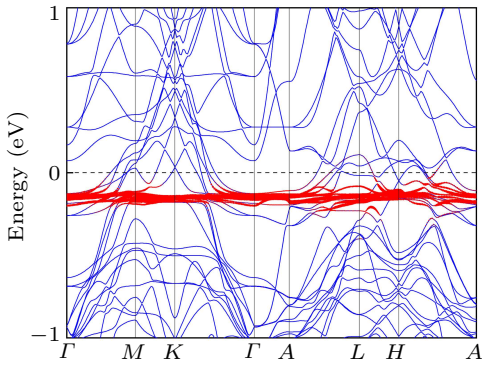


Fig. 8. The band structure when SOC is included. The bands with red color highlight the Yb 4f orbitals.

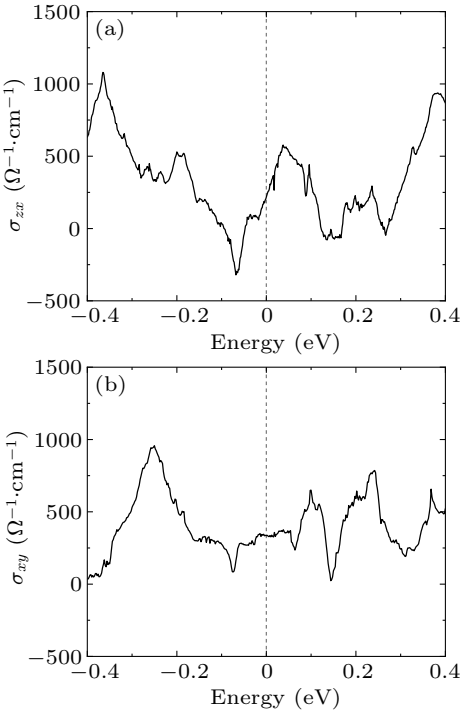


Fig. 9. Energy dependence of the calculated AHC when (a) $M_{\rm sat} \parallel ab$ plane and (b) $M_{\rm sat} \parallel c$ axis.

Figure 9 shows the energy dependence of the calculated intrinsic AHC with the different magnetization directions. When $M_{\rm sat}$ is parallel to the *ab* plane, $\sigma_{zx} = 217\ \Omega^{-1}\cdot\text{cm}^{-1}$ at the Fermi energy, and when $M_{\rm sat}$ is parallel to the *c* axis, $\sigma_{xy} = 335\ \Omega^{-1}\cdot\text{cm}^{-1}$ at the Fermi energy. The calculated value of σ_{zx} is comparable to the experimental but that of σ_{xy} is significantly larger.

We summarize the magnetic properties and the intrinsic AHCs of the FM and FF states when the magnetization of Mn spins is saturated in Table 1. Because most of the compounds are either AFM or strongly anisotropic FM, the FF state can not be obtained for all the compounds. Nevertheless, we notice that the highest AHC occurs in $LiMn_6Sn_6$ and $YbMn_6Sn_6$ which have the VEC less than 3+. In the RMn_6Sn_6 family, $YbMn_6Sn_6$ has the lowest magnetic ordering temperature but the largest saturated magnetization of Mn.

Ma *et al.*[19] suggested that the electronic structures of the FiM RMn_6Sn_6 (R = Gd to Er) resemble each other and the massive Dirac fermion is generally hosted in FM Mn kagome lattice when the Mn spins are polarized along the *c* axis. The intrinsic AHE of the FiM RMn_6Sn_6 (R = Gd to Er) can be attributed to the Berry curvature field of the massive Dirac fermion whose cone energy $E_{\rm D}$ and gap size Δ are determined by the de Gennes factor $dG = (g_J - 1)^2 J(J+1)$, where g_J is the Lande factor and J is the total angular momentum of the R^{3+} ion. If this Chern gap opening induced AHE mechanism is valid, the AHC shall be dependent on $\sqrt{dG}$. The above interpretation seems to be consistent with our observations of the nearly vanished intrinsic AHE for the FF state of YMn_6Sn_6 and $LuMn_6Sn_6$.

We summarize the intrinsic AHC with respect to the de Gennes factor for all RMn_6Sn_6 compounds in Fig. 10. The intrinsic AHCs for the heavy rare-earth FiM RMn_6Sn_6 are located in a brown zone, in which the magnitude approximately follows dG. The data points of the trivalent RMn_6Sn_6 with R being non-magnetic Y, Lu, and Sc are located in the blue zone in the lower left corner. On the other hand, $LiMn_6Sn_6$ and $YbMn_6Sn_6$ with less VEC show larger AHE and we label them in a magenta zone. The intrinsic AHCs considered here are $\sigma_{xy}^{\rm int}$ when $M_{\rm sat} \parallel c$ axis, while different mechanisms may play a role when $M_{\rm sat} \parallel ab$ plane, requiring further elaboration.

Table 1. Intrinsic AHCs of the RMn_6Sn_6 family with the magnetization of Mn atom saturated along the *c* axis and the *ab* plane in different categories. Data are taken from previous reports.[12–17,20,41,43,44] '/' means no data available. $T_{\rm M}$ denotes the magnetic ordering temperature. The magnetic structure and anisotropy are those at base temperatures. $M_{\rm s}$ is the saturated moments of Mn atoms at the lowest measurement temperature, usually at $T = 2$ K.

$R =$	Magnetism of R	Magnetic order	$\sigma_{xy}^{\rm int}$ ($\Omega^{-1}\cdot$cm^{-1})	$\sigma_{zx}^{\rm int}$ ($\Omega^{-1}\cdot$cm^{-1})	Valence	$T_{\rm M}$ (K)	Magnetic structure and anisotropy	$M_{\rm s}$ ($\mu_{\rm B}$ per Mn)
Yb	Non-magnetic	FM	146	308	2.6	277	easy plane	2.4
Mg			/	/	2	290	easy plane	1.88
Li			380	170	1	382	easy plane	2.4
Sc		AFM	65	/	3	384	flat spiral	1.75
Y			24	/		333	flat spiral	1.69
Lu			~ 0	/		353	flat spiral	1.59
Zr			/	/	4	580	helical	/
Hf			/	/		575	helical	/
Nd	magnetic	FM	145	120	3	350	easy axis	2.0
Sm			/	284		405	easy plane	2.1
Gd		FiM	140	32		435	easy plane	2.08
Tb			121	/		423	easy axis	2.4
Dy			60	/		393	conical	2.1
Ho			90	/		376	conical	2.3
Er		AFM	40	/		352	helimagnetic	2.2
Tm			/	/		347	helimagnetic	2.22

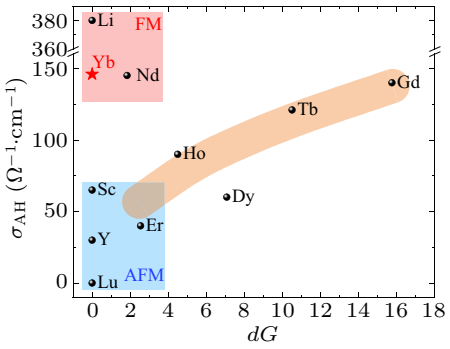


Fig. 10. Scaling of the intrinsic AHC with respect to the de Gennes factor. Data points in the brown zone are the FiM RMn$_6$Sn$_6$. Data points in the blue zone in the lower left corner are the AFM RMn$_6$Sn$_6$ whose intrinsic AHCs are relatively small. Data points in the magenta zone in the upper left corner are the FM RMn$_6$Sn$_6$ with less VEC whose intrinsic AHCs are relatively large.

In the band structure calculation for LiMn$_6$Sn$_6$, Chen *et al.*[41] suggested that the intrinsic AHC has a minimum value around 0.2 eV above the Fermi energy of LiMn$_6$Sn$_6$, which indicates that the trivalent RMn$_6$Sn$_6$ compounds shall have small AHC because their Fermi levels are lifted for about 0.23 eV by two extra electrons. This prediction seems to be consistent with the observations of small AHC in LuMn$_6$Sn$_6$ and YMn$_6$Sn$_6$. We notice a similar deep valley around 80 meV above the Fermi energy in our calculation for YbMn$_6$Sn$_6$ as well. On the other hand, the calculation also revealed a high peak of AHC around 0.15 eV above the Fermi energy of LiMn$_6$Sn$_6$. Although the Yb atom has an intermediate valence between 3+ and 2+, the AHC of YbMn$_6$Sn$_6$ is not as high as the prediction in band structure calculations.

This large discrepancy between the DFT calculation and experimental results may come from the over-simplified treatment of the intermediate valence of Yb atoms. A rigid band approximation may not be valid for the intermediate valence compounds. In YbMn$_6$Sn$_6$, the Yb atoms are nonmagnetic while the relatively large electronic specific heat coefficient γ indicates a high Kondo temperature T_K over several hundred Kelvins through scaling relations.[45–47] On the other hand, if the crystal field splitting does not lift the degeneracy when Yb atoms are Kondo screened, the multiplet ground state leads to a Kondo temperature of $T_K = \frac{R\ln 8}{\gamma_{Yb}-\gamma_{Lu}} = 219$ K, which is comparable to the T_C. This value is consistent with the inferred high T_K through scaling relations, which is comparable or even higher than T_C, indicating that the Yb ions have been fully Kondo screened at the FM state. Very recently, we have discovered large AHE in several heavy fermion ferromagnets. Or particular, the strong hybridization of 4f and conduction electrons in an FM Kondo lattice $CeCo_2As_2$ generates topological nodal loops near the Fermi level, which is a potent source of the Berry curvature field.[48] The intermediate valence of Yb has much stronger Kondo effects in YbMn$_6$Sn$_6$, but the influence of the Kondo effect on the AHE needs to be explored in the future. Previous studies on a series of solid solutions of polycrystalline YbMn$_6$Ge$_{6-x}$Sn$_x$ unveiled the change of the valence of Yb ions and even a quantum critical point when x equals 5.23.[24,26,45,47,49–51] The AHE of the series of YbMn$_6$Ge$_{6-x}$Sn$_x$ will be interesting.

5. Summary

We grew high-quality single crystals of YbMn$_6$Sn$_6$ which demonstrate an in-plane FM ordering of Mn moments at $T_C \sim$ 277 K. The Yb atom is nonmagnetic and the intermediate valence of Yb leads to a large $\gamma = 127$ mJ·mol^{-1}·K^{-2}. The intrinsic mechanism plays a crucial role in the AHE when the magnetization is along the c axis, leading to an enhanced intrinsic AHC as $\sigma_{xy}^{int} = 146.3\ \Omega^{-1}$·cm^{-1}, comparable to the FiM RMn$_6$Sn$_6$. The DFT calculations partially explain the experimental results, but the influence of the Kondo effect on the Berry curvature field and the AHE needs further exploration.

Acknowledgements

Project supported by the National Natural Science Foundation of China (Grant Nos. 12141002, 12225401, and 12274154), the National Key Research and Development Program of China (Grant No. 2021YFA1401902), the CAS Interdisciplinary Innovation Team, and the Strategic Priority Research Program of Chinese Academy of Sciences (Grant No. XDB28000000).

References

[1] Yin J X, Lian B and Hasan M Z 2022 *Nature* **612** 647
[2] Xu X, Yin J X, Qu Z and Jia S 2023 *Rep. Prog. Phys.* **86** 114502
[3] Norman M R 2016 *Rev. Mod. Phys.* **88** 041002
[4] Tang E, Mei J W and Wen X G 2011 *Phys. Rev. Lett.* **106** 236802
[5] Xu G, Lian B and Zhang S C 2015 *Phys. Rev. Lett.* **115** 186802
[6] Venturini G 2006 *Zeitschrift für Kristallographie - Crystalline Materials* **221** 511
[7] Fredrickson D C, Lidin S, Venturini G, Malaman B and Christensen J 2008 *JACS* **130** 8195
[8] Baranov N V, Gerasimov E G and Mushnikov N V 2011 *The Physics of Metals and Metallography* **112** 711
[9] Mazet T, Venturini G, Welter R and Malaman B 1998 *J. Alloys Compd.* **264** 71
[10] Mazet T, Welter R and Malaman B 1999 *J. Magn. Magn. Mater.* **204** 11
[11] Mazet T, Ihou-Mouko H, Marêché J F and Malaman B 2006 *Euro. Phys. J. B* **51** 173
[12] Venturini G, Fruchart D and Malaman B 1996 *J. Alloys Compd.* **236** 102
[13] Mazet T, Welter R and Malaman B 1999 *J. Alloys Compd.* **284** 54
[14] Malaman B, Venturini G, Chafik El Idrissi B and Ressouche E 1997 *J. Alloys Compd.* **252** 41
[15] Venturini G, Idrissi B E and Malaman B 1991 *J. Magn. Magn. Mater.* **94** 35
[16] Malaman B, Venturini G, Welter R, Sanchez J, Vulliet P and Ressouche E 1999 *J. Magn. Magn. Mater.* **202** 519
[17] Yin J X, Ma W, Cochran T A, Xu X, Zhang S S, Tien H J, Shumiya N, Cheng G, Jiang K, Lian B, Song Z, Chang G, Belopolski I, Multer D, Litskevich M, Cheng Z J, Yang X P, Swidler B, Zhou H, Lin H, Neupert T, Wang Z, Yao N, Chang T R, Jia S and Zahid Hasan M 2020 *Nature* **583** 533

[18] Xu X, Yin J X, Ma W, Tien H J, Qiang X B, Reddy P V S, Zhou H, Shen J, Lu H Z, Chang T R, Qu Z and Jia S 2022 *Nat. Commun.* **13** 1197

[19] Ma W, Xu X, Yin J X, Yang H, Zhou H, Cheng Z J, Huang Y, Qu Z, Wang F, Hasan M Z and Jia S 2021 *Phys. Rev. Lett.* **126** 246602

[20] Ma W, Xu X, Wang Z, Zhou H, Marshall M, Qu Z, Xie W and Jia S 2021 *Phys. Rev. B* **103** 235109

[21] Ghimire N J, Dally R L, Poudel L, Jones D C, Michel D, Magar N T, Bleuel M, McGuire M A, Jiang J S, Mitchell J F, Lynn J W and Mazin I I 2020 *Science Advances* **6** eabe2680

[22] Wang Q, Neubauer K J, Duan C, Yin Q, Fujitsu S, Hosono H, Ye F, Zhang R, Chi S, Krycka K, Lei H and Dai P 2021 *Phys. Rev. B* **103** 014416

[23] Xia S Q and Bobev S 2006 *Acta Crystallographica Section E* **62** i7–i9

[24] Eichenberger L, Venturini G, Malaman B, Nataf L, Baudelet F and Mazet T 2017 *J. Alloys Compd.* **695** 286

[25] Magnette A, Vernière A, Venturini G, Eichenberger L, Malaman B and Mazet T 2018 *J. Magn. Magn. Mater.* **458** 19

[26] Mazet T, Malterre D, François M, Eichenberger L, Grioni M, Dallera C and Monaco G 2015 *Phys. Rev. B* **92** 075105

[27] Lv B, Zhong R, Luo X, Ma S, Chen C, Wang S, Luo Q, Gao F, Fang C, Ren W and Zhong Z 2023 *J. Alloys Compd.* **957** 170356

[28] Canfield P C and Fisk Z 1992 *Philos. Mag. B* **65** 1117

[29] Wang B, Yi E, Li L, Qin J, Hu B F, Shen B and Wang M 2022 *Phys. Rev. B* **106** 125107

[30] Kresse G and Furthmüller J 1996 *Computational Materials Science* **6** 15

[31] Kresse G and Furthmüller J 1996 *Phys. Rev. B* **54** 11169

[32] Blöchl P E 1994 *Phys. Rev. B* **50** 17953

[33] Perdew J P, Burke K and Ernzerhof M 1996 *Phys. Rev. Lett.* **77** 3865

[34] Anisimov V I, Zaanen J and Andersen O K 1991 *Phys. Rev. B* **44** 943

[35] Mostofi A A, Yates J R, Pizzi G, Lee Y S, Souza I, Vanderbilt D and Marzari N 2014 *Comput. Phys. Commun.* **185** 2309

[36] Wu Q, Zhang S, Song H F, Troyer M and Soluyanov A A 2018 *Comput. Phys. Commun.* **224** 405

[37] Stewart G R 1984 *Rev. Mod. Phys.* **56** 755

[38] Zeng C, Yao Y, Niu Q and Weitering H H 2006 *Phys. Rev. Lett.* **96** 037204

[39] Tian Y, Ye L and Jin X 2009 *Phys. Rev. Lett.* **103** 087206

[40] Li M, Wang Q, Wang G, Yuan Z, Song W, Lou R, Liu Z, Huang Y, Liu Z, Lei H, Yin Z and Wang S 2021 *Nat. Commun.* **12** 3129

[41] Chen D, Le C, Fu C, Lin H, Schnelle W, Sun Y and Felser C 2021 *Phys. Rev. B* **103** 144410

[42] Liu Z, Zhao N, Li M, Yin Q, Wang Q, Liu Z, Shen D, Huang Y, Lei H, Liu K and Wang S 2021 *Phys. Rev. B* **104** 115122

[43] Zhang L 2005 *Unusual magnetic behavior of some rare-earth and manganese compounds* Ph. D. thesis (University of Amsterdam)

[44] Asaba T, Thomas S M, Curtis M, Thompson J D, Bauer E D and Ronning F 2020 *Phys. Rev. B* **101** 174415

[45] Eichenberger L, Malterre D, Malaman B and Mazet T 2017 *Phys. Rev. B* **96** 155129

[46] Kummer K, Geibel C, Krellner C, Zwicknagl G, Laubschat C, Brookes N B and Vyalikh D V 2018 *Nat. Commun.* **9** 2011

[47] Eichenberger L, Magnette A, Malterre D, Sibille R, Baudelet F, Nataf L and Mazet T 2020 *Phys. Rev. B* **101** 020408

[48] Cheng Z J, Huang Y, Zheng P, Chen L, Cochran T A, Hu H, Yin J X, Yang X P, Hossain M S, Zhang Q, Belopolski I, Liu R, Cheng G, Hashimoto M, Lu D, Xu X, Zhou H, Ma W, Chang G, Yao N, Yin Z, Hasan M Z and Jia S 2023 Preprint 2302.12113

[49] Mazet T, Ihou-Mouko H, Ryan D H, Voyer C J, Cadogan J M and Malaman B 2010 *J. Phys. Condens. Matter* **22** 116005

[50] Mazet T, Malterre D, François M, Dallera C, Grioni M and Monaco G 2013 *Phys. Rev. Lett.* **111** 096402

[51] Haraux P, Eichenberger L, Diop L and Mazet T 2022 *Solid State Commun.* **341** 114551